Variable thermal expansion in $CuInP_2S_6$

Chuangye Song,[1,2,*] Song Zhou,[2,3] Xueyun Wang,[4] Xiaoyue He,[1] and Kehui Wu[1,2,3,5,†]

[1]*Songshan Lake Materials Laboratory, Dongguan, Guangdong 523808, China*
[2]*Institute of Physics, Chinese Academy of Sciences, Beijing 100190, China*
[3]*School of Physics, University of Chinese Academy of Sciences, Beijing 100049, China*
[4]*School of Aerospace Engineering, Beijing Institute of Technology, Beijing 100081, China*
[5]*Interdisciplinary Institute of Light-Element Quantum Materials and Research Center for Light-Element Advanced Materials, Peking University, Beijing 100871, China*

(Received 25 August 2022; revised 21 December 2022; accepted 22 December 2022; published 6 January 2023)

Materials normally exhibit positive thermal expansion, and materials with negative thermal expansion coefficient are of great interest for both fundamental study and applications such as high-precision microscale actuators, thermal expansion compensators, etc. Here, the coefficients of linear thermal expansion (α_L) along the c axis of the layered ferroelectric $CuInP_2S_6$ have been measured. In the single-crystalline bulk specimen, α_L exhibits large negative thermal expansion up to $-20.05 \times 10^{-6}\,K^{-1}$ in the temperature range below 150 K. In contrast to the bulk, exfoliated ultrathin $CuInP_2S_6$ flakes exhibit an overall positive $\alpha_L \sim 26.8 \times 10^{-6}\,K^{-1}$. The thickness-dependent thermal expansion of $CuInP_2S_6$ crystal may facilitate the design of van der Waals heterostructures and ferroelectric devices with tunable thermal responses.

DOI: 10.1103/PhysRevB.107.045406

I. INTRODUCTION

Solid materials exhibit thermal expansion that can be described by the linear thermal expansion coefficient (TEC), $\alpha_L = (1/L_0)(dL/dT)$, or volume TEC $\alpha_V = (1/V_0)(dV/dT)$, which describe the change of the material size in length L or volume V with temperature [1,2]. In general, most materials exhibit positive thermal expansion (PTE), i.e., expand their volume with increasing temperature [3]. Negative thermal expansion (NTE) [4–8] is an unusual phenomenon which can arise from electronic or magnetic effects, and is often employed in the thermal expansion engineering. Combining PTE and NTE materials may provide potential opportunities to design heterostructures with controllable thermal response. So far, controllable thermal expansion in two-dimensional (2D) van der Waals (vdW) materials has been rarely reported, despite that the interest in 2D materials and flexible devices based on 2D heterostructures is increasing rapidly.

$CuInP_2S_6$ (CIPS) is a material of intensive research interest in recent years, due to its van der Waals layered structure as well as rich properties including ferroelectricity above room temperature [9–12], photovoltaic effect [13], giant negative piezoelectric/electrostrictive coefficient [14,15], and room-temperature electrocaloric effect [16]. It is thus a promising candidate material for developing high-performance electromechanical and electrocaloric devices.

In this work, we report that the bulk crystalline CIPS exhibits anomalous and large negative linear thermal expansion coefficient at the temperature below 150 K. The α_L up to $-20.05 \times 10^{-6}\,K^{-1}$ in the c direction is determined by using temperature-dependent x-ray diffraction (XRD). In the meantime, a low-temperature microcracking is identified in the single-crystal specimen that can reversibly self-heal to the initial state during warming. In contrast to NTE in the bulk, the exfoliated ultrathin CIPS flakes exhibit an overall positive $\alpha_L \sim 26.8 \times 10^{-6}\,K^{-1}$. The anomalous thermal expansion of the ultrathin and bulk CIPS is further evidenced by the low-temperature Raman spectrum. The possible mechanism of the variable NTE is discussed.

II. RESULTS AND DISCUSSION

The CIPS has a layered crystal structure as depicted in Fig. 1(a), in which the sulfur atoms are covalently interconnected to form a framework, the Cu, In, and P-P pair atoms fill in the sulfur cages with a triangular pattern, respectively. Each $(P_2S_6)^{4-}$ unit consists of two distorted trigonal PS_3 pyramids bound by a P-P bond. Symmetry breaking generated by the antiparallel displacement of Cu and In sublattices occurs from nonpolar $C2/c$ to polar Cc, resulting a spontaneous polarization perpendicular to the layer planes [17]. The room-temperature XRD characterization of CIPS has been performed. As shown in Fig. 1(b), a set of strong peaks (black) at 13.59°, 27.36°, 41.55°, 56.45°, and 72.5° are assigned to (002), (004), (006), (008), and (0010), respectively, confirming that the CIPS crystal has the surface in the ab plane. Note that another set of broad peaks (green) at 43.36°, 50.447°, and 71.168° are assigned to the sample holder made from stainless steel.

Temperature-dependent XRD measurement (D8 Discover, Bruker) has been performed with the sample initially cooled to 12 K, and the XRD spectra measured during warming up

*cyesong@iphy.ac.cn
†khwu@iphy.ac.cn

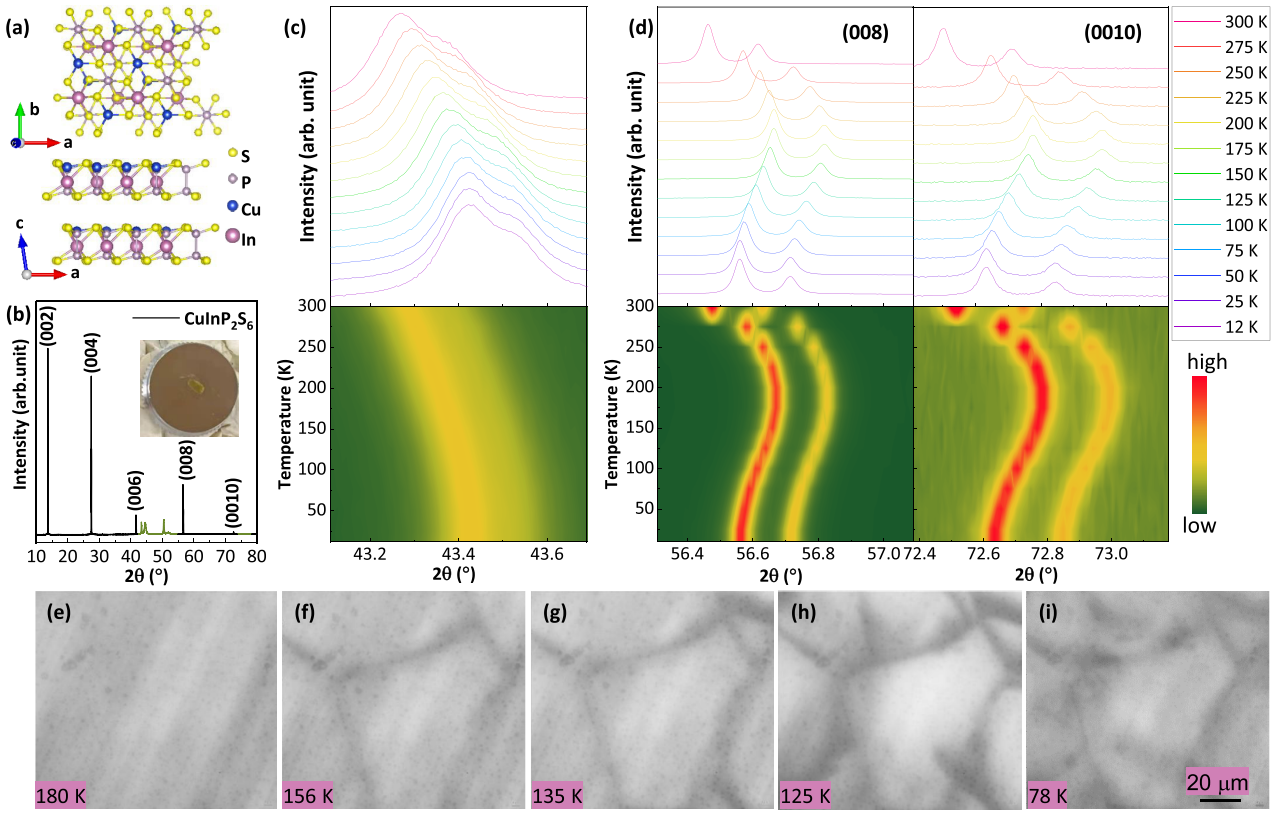

FIG. 1. (a) Structural model of CIPS in top and side views. (b) Typical XRD spectrum of CIPS. The inset is an optical picture of the CIPS crystal placed on a sample holder. (c) Temperature-dependent XRD spectra of the sample holder during the warming process. (d) Temperature-dependent (008)- and (0010)-XRD spectra of the CIPS bulklike crystal during the warming process. (e)–(i) Temperature-dependent CIPS morphology imaged by optical microscopy upon cooling.

the sample to room temperature. A slice of high-quality CIPS crystal, with size of 4.0 mm × 2.4 mm as shown in the inset of Fig. 1(b), is placed on a stainless-steel holder; its optical image shows the defect-free surface in large area. The XRD data of both sample holder and CIPS are collected between 12 and 300 K. Upon warming at a rate of 3 K/min, the diffraction peak of the sample holder [Fig. 1(c)] continuously moves to the lower angle. Note that the shoulders result from the K_α doublet of the incident x ray, consisting of K_{α_1} and K_{α_2} radiation. According to Bragg's law, $n\lambda = 2d\sin\theta$, smaller diffraction angle means larger d, confirming a normal positive linear-thermal expansion in the stainless-steel sample holder. In contrast, the diffraction peaks of CIPS firstly move to higher diffraction angle, and then back to the lower angle during the warming process [Fig. 1(d)]. It exhibits an anomalous evolution, i.e., the c lattice of CIPS contracts with increasing temperature below $T = 150$ K, and then expands with further increasing the temperature up to $T = 300$ K. An unexpected NTE in low-temperature range is thus identified. The low-temperature NTE in this CIPS crystal is further corroborated with the optical imaging. As shown in Fig. 1(e), the sample has a uniform contrast at $T = 180$ K, indicating a homogeneous CIPS sample. However, microcracks begin to form with lowering the temperature; the contrast and density of the microcracks increase at low temperature, indicating significant lattice deformation. The microcracks can be self-healed during the warming process (Fig. S1 of the Supplemental Material [18]), indicating that the lattice deformation is reversible.

Interestingly, in addition to the XRD peaks with NTE, some of our samples show another set of XRD peaks, with positive thermal expansion, splitting from the same set of XRD peaks with lowering the temperature. The corresponding temperature-dependent XRD spectra with (001)-diffraction peaks are shown in Fig. 2(b). The strong signals exhibit similar thermodynamic as that in bulk crystal [see Fig. 1(d)], where c lattice first contracts and then expands during the warming process. Here, we denote this set of signals as bulk crystal phase. Interestingly, another set of XRD patterns, clearly with much lower intensity, emerges and moves to larger angle as the temperature decreases, indicating positive thermal expansion. The extracted c-lattice parameters from Rietveld refinements of these two distinct sets of diffraction signals are present in Fig. 2(c). The lattice change and subsection linear fitting of the bulk-crystal phase are analyzed in Figs. 2(d) and 2(e). The $\alpha_L = (\Delta L/\Delta T)/L_{300\,\mathrm{K}}$ exhibits a negative value reaching up to $-20.05 \times 10^{-6}\,\mathrm{K}^{-1}$, which is comparable to the giant NTE reported in alloy compounds [19]. Figure 2(f) plots the changes of c lattice with temperature as extracted from the set of weak signals, and a positive thermal expansion coefficient of $\alpha_L \sim 26.8 \times 10^{-6}\,\mathrm{K}^{-1}$ is deduced.

Carefully comparing the samples in Fig. 2 with that in Fig. 1 in optical microscope, we find noticeable nanoflakes

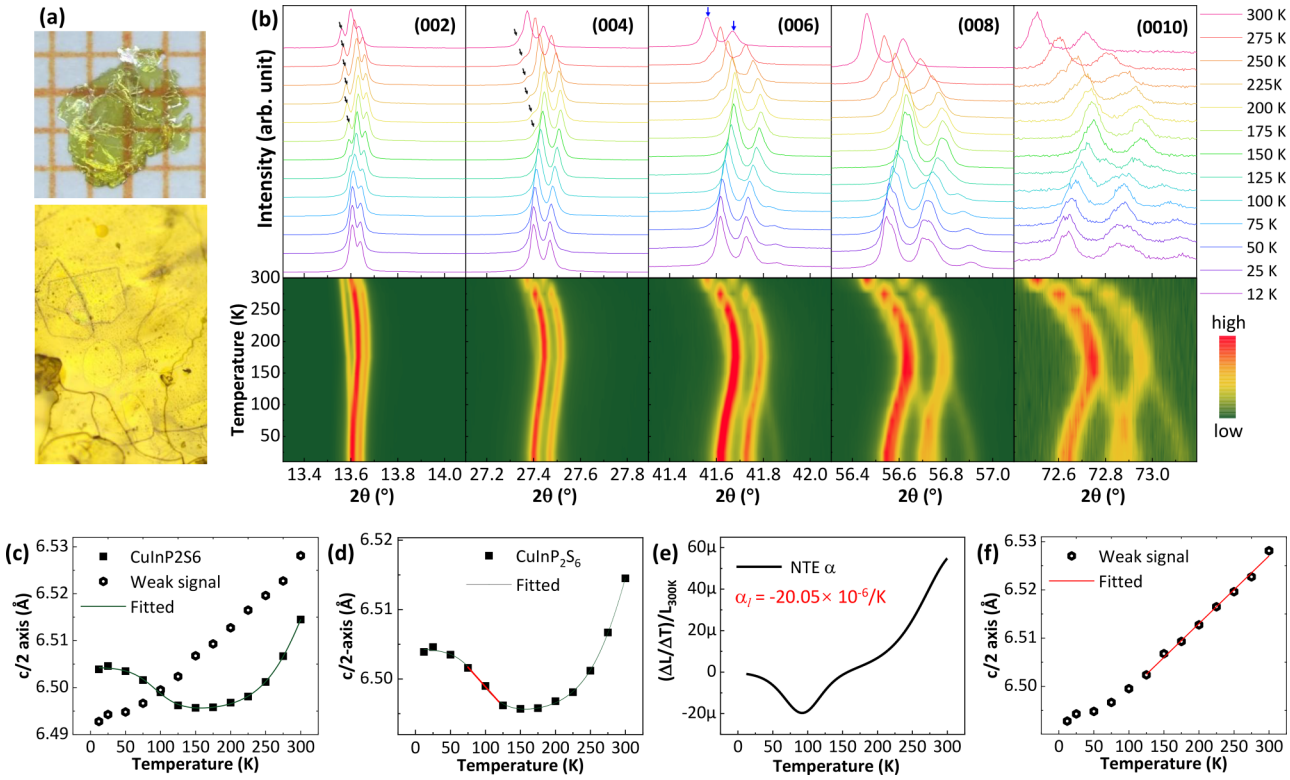

FIG. 2. (a) Top panel: picture of CIPS bulk crystal placed on a millimeter grid. Bottom panel: Enlarged view of the CIPS crystal imaged by optical microscope, revealing the coexistence of nanoflakes on the surface. (b) Temperature-dependent (002)-, (004)-, (006)-, (008)-, and (0010)-XRD spectra during the warming process; the diffraction angle range of each peak is 0.8°. Two neighboring doublet peaks of bulk CIPS crystal are marked with blue arrows, and the weak peaks from the flakes are marked with black arrows. (c) Extracted c-lattice parameters from Rietveld refinements of the XRD data, where two distinct sets of diffraction signals are present, strong (square) and weak (circle). (d) Lattice parameter and linear fitting of the bulk crystal phase as extracted from the data shown in Fig. 1(d). (e) Linear thermal expansion $(\Delta L/\Delta T)/L_{300\,\mathrm{K}}$ extracted from (d). (f) Lattice change and subsection linear fitting of the set of diffraction signals with weak intensity.

on the surface and edges of the CIPS crystal [see Fig. 2(a)]. Considering the relative weak diffraction signal, the weaker set of XRD peaks highly possibly come from the randomly distributed nanoflakes with few layers. As shown in Fig. S2 of the Supplemental Material [18], for the (002) peak, the weak and strong streaks do not coincide at low temperature. The peak position of the strong one is indicated with solid arrows, and actually separates with the low-temperature evolution tendency of the weak one (dashed arrow). Due to the small difference (∼0.04°) between the strong and weak peaks, it is a little difficult to distinguish them at low temperature. With the increase of the diffraction order n, the separation between neighboring doublet peaks of CIPS grows. However, the relative location of the weak and strong diffraction peaks changes due to $d_{\mathrm{flake}} \neq d_{\mathrm{bulk}}$; the details are discussed as follows: In the x-ray diffraction measurement, diffraction occurs at an angle 2θ, as defined by Bragg's law: $2d\sin\theta = n\lambda$, where n is an integer denoting the order of diffraction, d is the lattice spacing of crystal planes along c axes, θ is the diffraction angle, and λ is the x-ray wavelength. K_α doublet incident x ray consists of K_{α_1} and K_{α_2} radiation, whose wavelengths are λ_1 and λ_2, respectively. The separation between neighboring doublet peaks of the bulk CIPS crystal (strong streaks), as marked by blue arrows in Fig. 2(b), is $\sin\theta_1 - \sin\theta_2 = \frac{\lambda_1-\lambda_2}{2d_{\mathrm{bulk}}}$ n. The separation expands with the increase of the diffraction order n; for example, the separation of (0010) peak is much larger than that of the (002) peak. Accordingly, the separation between neighboring doublet peaks of the CIPS flakes (weak streaks) is $\sin\theta_1 - \sin\theta_2 = \frac{\lambda_1-\lambda_2}{2d_{\mathrm{flake}}}$ n. At room temperature, we can distinguish the weak streak from the strong one at $n = 2$. Due to $d_{\mathrm{flake}} > d_{\mathrm{bulk}}$ at $T = 300\,\mathrm{K}$, the separation between neighboring doublet peaks of the bulk CIPS crystal expands faster than that of the ultrathin flakes when increasing n. With the increase of diffraction order n from 2 to 10, the doublet diffraction peaks of the bulk CIPS overlap and cover the weak peaks from the ultrathin flakes as marked by black arrows in Fig. 2(b); At low temperature (e.g., $T = 12\,\mathrm{K}$), the weak streak of the ultrathin CIPS almost mixes with the strong one at $n = 2$. Actually, they do not coincide (see Fig. S2 of the Supplemental Material [18] for details). Due to $d_{\mathrm{flake}} \leqslant d_{\mathrm{bulk}}$ here, the separation between neighboring doublet peaks of the ultrathin CIPS flakes expands faster than that of the bulk crystal. With the increase of diffraction order n from 2 to 10, the weak peaks from the ultrathin flakes expand much faster and move towards higher diffraction angle. Thus, the diffraction peaks of the bulk CIPS separate with the weak streak obviously at high diffraction orders [see Fig. 2(b) for details]. In fact, the set of signals with lower intensity could disappear by carefully removing the residual nanoflakes, which supports the above assumption.

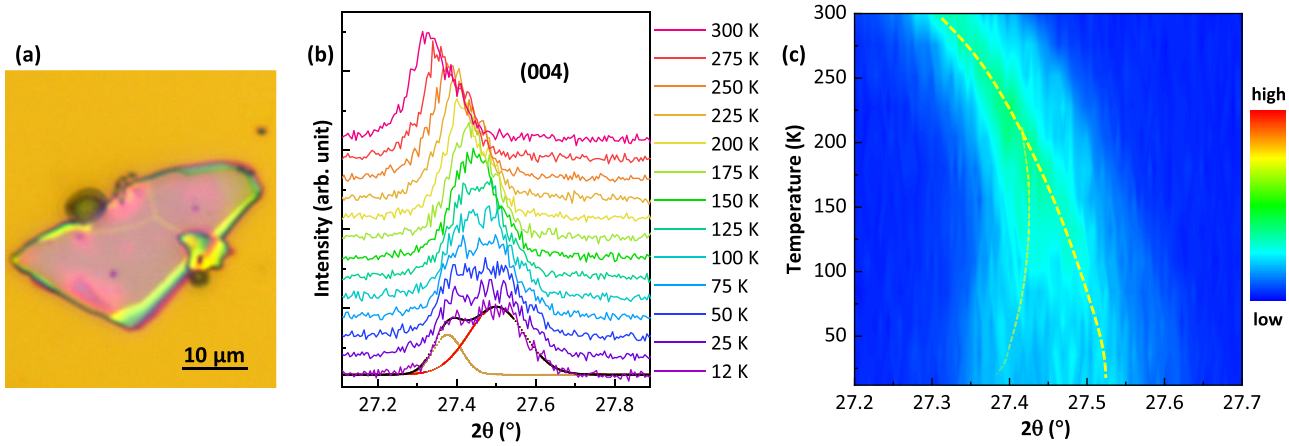

FIG. 3. (a) Optical image of a 30.3-nm-thick CIPS nanoflake obtained by liquid exfoliation; a small amount of thick CIPS nanoflakes inevitably coexist with the few-layer ones. (b) Temperature dependence of XRD data around the (004) peak (offset for display purposes); the doublet structure of the XRD curve at $T = 12$ K is fitted. (c) Two-dimensional map display of that in (b).

To further prove our hypothesis, we have prepared sample with few-layer CIPS nanoflakes in large quantity by liquid exfoliation [20]. As shown in Fig. 3(a), the exfoliated CIPS nanoflakes with small size are imaged by optical microscopy. It should be noted that a small amount of thick CIPS nanoflakes inevitably coexist with the few-layer ones (see Fig. S3 of the Supplemental Material [18] for details). The XRD signal from this sample is much weaker due to the dramatically reduced sample volume, but still clearly observable. The temperature-dependent (004) peak is shown in Fig. 3(b) and the corresponding 2D map shown in Fig. 3(c); the TOPAS 6 software is used for the Le Bail fitting of the XRD data. Upon cooling the sample from room temperature, the single peak moves to higher diffraction angle, indicating the contraction along the c axis, while the peak broadens and splits into two peaks with further decreasing temperature below $T = 150$ K: one moving to lower angle (negative α), the other to higher angle (positive α) with relatively higher intensity. The phenomenon is the same as the measurement in Fig. 2, but the change of the much weaker signal in Fig. 2(b) to a comparative one in Fig. 3 is deterministically identified, which can be attributed to the dramatically increased proportion of the nanoflakes in the liquid-exfoliated CIPS. In addition, temperature-dependent optical imaging of the ultrathin nanoflakes shows uniform contrast and no microcrack is observed. Thus, our experiments prove that NTE in CIPS occurs only in bulklike crystals, while ultrathin nanoflakes show positive thermal expansion. The critical thickness for NTE is roughly estimated to be between 40 and 70 nm according to the height measurement by atomic force microscopy (AFM). So far, a precise determination of the critical thickness is not available due to the difficulties in the preparation of samples with continuously varied thickness.

The thermal property of material is associated with the phonon modes, which can be studied by Raman spectra. We measured the temperature-dependent Raman spectra of CIPS bulk crystal using a Horiba LabRAM HR Evolution instrument during the cooling process; the laser excitation wavelength for the Raman spectroscopy measurement is $\lambda = 532$ nm and the sample is cooled by liquid nitrogen. Figure 4(a) presents the spectra, which exhibit the typical features of CIPS as previously reported [21–23]. The Raman peaks at high frequency mainly originate from the $(P_2S_6)^{4-}$ triangle deformation vibration, including P-P pair off-centering, PS_3 group twists, P-S distance, and S-P-S angle changes. The two major peaks at 267 and 376 cm^{-1} are labeled as peak 1 and peak 2, respectively. The peak 1 ($\omega_1 = 267\ cm^{-1}$) accounts for the S-P-S deformation mode. It is closely related to distortions within the S_6 cage occupied by Cu and In atoms. The peak 2 ($\omega_2 = 376\ cm^{-1}$) can be ascribed to the internal P-P stretching vibration, i.e., the antiphase motions of the PS_3 groups stretch the P-P bond [24]. The intensity of both peak 1 (I_1) and peak 2 (I_2) monotonically increase with the decrease of temperature; especially, the increasing rates are slightly enhanced below $T = 150$ K. It is worth noting that the intensity ratio of peak 1 and peak 2: I_1/I_2 first decreases upon cooling from room temperature and then increase below $T = 150$ K [see Fig. 4(b)], indicating that the S-P-S deformation has a relatively higher increasing rate than the P-P stretching vibration modes in the P_2S_6 frameworks at low temperature. It may be possible that there exists a correlation between S-P-S deformation and P-P stretching vibration modes. Importantly, with the decrease of temperature, both peak 1 and peak 2 first shows a typical blueshift, and then turn to a redshift around $T = 150$ K with further decreasing the temperature, as shown in Figs. 4(c) and 4(d). The vibration frequencies of peak 1 and peak 2 are extracted in Figs. 4(e) and 4(f), both of which exhibit obvious evolution from blueshift to redshift upon cooling.

The analysis of vibration modes in the P_2S_6 triangle could account for the anomalous thermal expansion in CIPS bulk crystal. With the decrease of temperature from room temperature, the c lattice first contracts, i.e., the P-P bond length shortens and the S-P-S angle change weakens. Correspondingly, the vibration modes accounting for P-P bond stretching (peak 2) and S-P-S deformation gradually harden; both of them exhibit a blueshift. With further decreasing the temperature below $T = 150$ K, the c lattice starts to expand, i.e., the P-P bond length elongates and the S-P-S angle change intensifies. Correspondingly, the vibration modes accounting

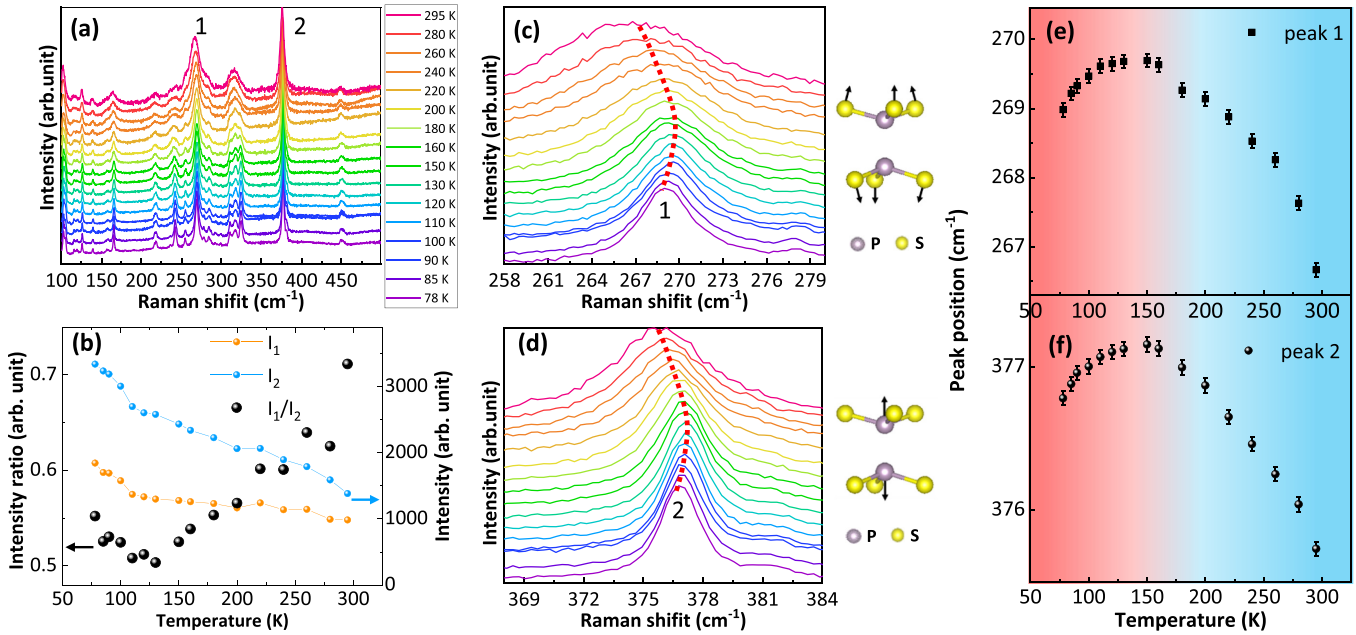

FIG. 4. (a) Raman spectra of CIPS bulk crystal for different temperatures. Two major peaks at approximately 267 and 376 cm^{-1} are marked as peak 1 and peak 2, respectively. (b) Temperature-dependent intensity of peak 1 (I_1) and peak 2 (I_2) as well as intensity ratio (I_1/I_2) as a function of temperature. (c) Enlarged view of peak 1; the right panel is the schematic of atomic vibration mode. (d) Enlarged view of peak 2; the right panel is the schematic of atomic vibration mode. (e) Temperature-dependent Raman frequency of peak 1. (f) Temperature-dependent Raman frequency of peak 2.

for P-P bond stretching (peak 2) and S-P-S deformation (peak 1) gradually soften; both of them exhibit a redshift. By direct comparison of the Raman spectra with XRD patterns, we propose that anomalous linear thermal expansion at low temperature can be attributed to the deformation of P_2S_6 basal triangles consuming open spaces in the monoclinic structure at low temperature.

The thickness dependence of the NTE is further supported by Raman-scattering measurements performed on the ultrathin CIPS nanoflakes [Fig. 5(a)]. In this case, the intensity ratio of peak 1 and peak 2: I_1/I_2 monotonically decreases in the temperature range 300 $\sim$ 78 K [see Fig. 5(b)], indicating the synchronous evolution of the S-P-S deformation and P-P stretching vibration modes. With the decrease of temperature, both peak 1 [Fig. 5(c)] and peak 2 [Fig. 5(d)] shift to higher wave number. The corresponding vibration frequencies of peak 1 and peak 2 are extracted in Figs. 5(e) and 5(f), which exhibit a typical blueshift with lowering the temperature, resulting in hardened vibration modes, i.e., the P-P bond length shortens and the S-P-S angle change weakens. Thus, the respective vibration modes and linear thermal expansion of the CIPS nanoflakes determined by Raman spectra and XRD patterns have the similar monotonic evolution tendency. Based on the above discussion, we can identify that the thermomechanics can change dramatically when reducing the bulk CIPS into ultrathin nanoflakes.

The last issue here is why the observed NTE has a thickness dependence, i.e., why it only occurs in bulklike samples but absents itself in ultrathin flakes. In the bulk CIPS, the transition from PTE to NTE occurs below $T = 150$ K, which corresponds to the onset of dipolar glass phase [25,26] ($T = 153$ K); it is consistent with our dielectric measurement as shown in Figs. S4(a) and S4(b) of the Supplemental Material [18]. The dipolar glass phase is due to the disorder in copper sublattice: the disordered copper ions can distribute and hop between more than three positions (nonpolar with Cu close to octahedron centers; low polarization with Cu at off-centered positions; and high polarization with Cu penetrating into the interlayer space). At temperature below $T = 153$ K, the copper-ion hopping freezes and exhibits 100% copper-ion ordering. The copper sublattice tends to be frozen at low temperature; thus, the NTE in CIPS may arise from S octahedral rotation and deformation via altering the octahedral connectivity and shape, possibly accompanied with the intersite Cu-In charge transfer mediated by the corner-sharing S atoms. The octahedra rotation and deformation may also explain the microcracks of bulk CIPS on cooling [Figs. 1(e)–1(i)]. As shown in Fig. S4(c) of the Supplemental Material [18], the Raman spectrum reveals the cation (Cu^+) transition around 320 cm^{-1}, which emerges as a broad peak around room temperature ($T = 300$ K). Interestingly, the broad peak begins to evolve into three distinct peaks around $T = 150$ K, and the peak width at half maximum gradually decrease with further cooling the sample to $T = 78$ K. The three Raman-scattering peaks also imply the existence of Cu ordering states at low temperature, i.e., nonpolar with Cu close to octahedron centers, low polarization with Cu at off-centered positions, and high polarization with Cu penetrating into the interlayer (vdW gap) space, which help us understand the origin of the low-temperature NTE in bulk CIPS.

Importantly, the NTE to PTE transition occurs below a certain thickness via exfoliation. As to the exfoliated CIPS flakes, some thick flakes (>100 nm in thickness) inevitably coexist with the thin ones, i.e., there indeed exists a wide

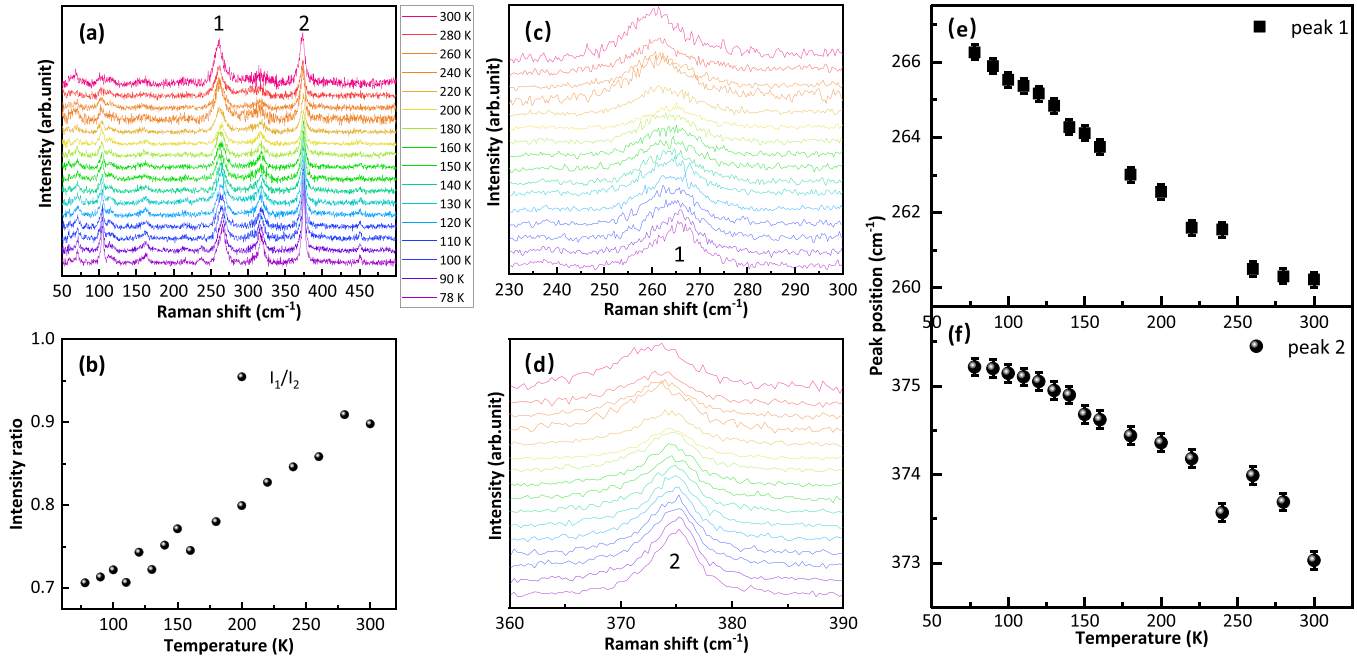

FIG. 5. (a) Raman spectra of a 30.3-nm-thick CIPS nanoflake for different temperatures. Two major peaks at approximately 267 and 376 cm^{-1} are marked as peak 1 and peak 2, respectively. (b) Intensity ratio (I_1/I_2) as a function of temperature. (c) Enlarged view of peak 1. (d) Enlarged view of peak 2. (e) Temperature-dependent Raman frequency of peak 1. (f) Temperature-dependent Raman frequency of peak 2.

range of thickness even though most of the flakes are similar to that in Fig. 3(a) (30 nm in thickness). Based on the phenomenon that the dramatically increased proportion of the ultrathin nanoflakes in the liquid-exfoliated CIPS makes the very weak signal from the flakes in Fig. 2(b) a stronger one in Fig. 3, it suggests that there is an abrupt change in the thermal expansion coefficient above some critical thickness. In addition, Li *et al.* reported the enhanced bulk photovoltaic effect [13]; they found a dramatic decrease in the photocurrent density when the thickness of CIPS flake exceeds 80 nm. Deng *et al.* reported a critical thickness between 90 and 100 nm, below which the in-plane polarization disappears [10]. They attribute this behavior to a structural phase transition from monoclinic (thick) to trigonal (thin) structure. Thus, the ultrathin CIPS flake with trigonal structure may possess more stable thermal stability at low temperature compared with that of the monoclinic phase. The copper-ion ordering below $T = 150$ K in the bulk CIPS with monoclinic structure may have a close relationship with the negative linear thermal expansion along the c axis.

III. CONCLUSIONS

In our work, the linear thermal expansion of c lattice changes from a negative value in the bulk crystal to a positive value in the ultrathin 2D flakes via mechanical exfoliation. The bulklike crystal demonstrates a large negative linear thermal expansion coefficient up to $\alpha_L = -20.05 \times 10^{-6}\,K^{-1}$ at low temperature, while a pure positive $\alpha_L \sim 26.8 \times 10^{-6}\,K^{-1}$ could be realized when exfoliating the CIPS crystal into ultrathin nanoflakes. The variable thermal expansion of the van der Waals CIPS crystal can facilitate the alternative integration for 2D advanced electronic devices and spaceflight engineering working with extreme temperature fluctuations.

ACKNOWLEDGMENTS

This work was supported by the Ministry of Science and Technology of China (Grant No. 2021YFA1400502), National Natural Science Foundation of China (Grants No. 11825405 and No.1192780039), the Strategic Priority Research Program of the Chinese Academy of Sciences (Grant No. XDB30000000), the China Postdoctoral Science Foundation (Grant No. 2020M670502), and the Guangdong Basic and Applied Basic Research Foundation (Grant No. 2021A1515010030). We are grateful for the help of Xiaohuan Lin and Fan Dang from Songshan Lake Materials Laboratory in the data analysis.

The authors declare no competing interests.

[1] W. Miller, C. W. Smith, D. S. Mackenzie, and K. E. Evans, J. Mater. Sci. **44**, 5441 (2009).

[2] R. Mittal, M. K. Gupta, and S. L. Chaplot, Prog. Mater. Sci. **92**, 360 (2018).

[3] J. S. Dugdale and D. K. C. MacDonald, Phys. Rev. **89**, 832 (1953).

[4] R. Huang, Y. Liu, W. Fan, J. Tan, F. Xiao, L. Qian, and L. Li, J. Am. Chem. Soc. **135**, 11469 (2013).

[5] E. Pachoud, J. Cumby, C. T. Lithgow, and J. P. Attfield, J. Am. Chem. Soc. **140**, 636 (2018).
[6] M. S. Senn, A. Bombardi, C. A. Murray, C. Vecchini, A. Scherillo, X. Luo, and S. W. Cheong, Phys. Rev. Lett. **114**, 035701 (2015).
[7] K. Takenaka, Y. Okamoto, T. Shinoda, N. Katayama, and Y. Sakai, Nat. Commun. **8**, 14102 (2017).
[8] D. Wendt, E. Bozin, J. Neuefeind, K. Page, W. Ku, L. Wang, B. Fultz, A. V. Tkachenko, and I. A. Zaliznyak, Sci. Adv. **5**, eaay2748 (2019).
[9] J. A. Brehm, S. M. Neumayer, L. Tao, A. O'Hara, M. Chyasnavichus, M. A. Susner, M. A. McGuire, S. V. Kalinin, S. Jesse, and P. Ganesh, Nat. Mater. **19**, 43 (2020).
[10] J. Deng, Y. Liu, M. Li, S. Xu, Y. Lun, P. Lv, T. Xia, P. Gao, X. Wang, and J. Hong, Small **16**, 1904529 (2020).
[11] F. Liu, L. You, K. L. Seyler, X. Li, P. Yu, J. Lin, X. Wang, J. Zhou, H. Wang, H. He, S. T. Pantelides, W. Zhou, P. Sharma, X. Xu, P. M. Ajayan, J. Wang, and Z. Liu, Nat. Commun. **7**, 12357 (2016).
[12] S. Zhou, L. You, H. Zhou, Y. Pu, Z. Gui, and J. Wang, Front. Phys. **16**, 13301 (2020).
[13] Y. Li, J. Fu, X. Mao, C. Chen, H. Liu, M. Gong, and H. Zeng, Nat. Commun. **12**, 5896 (2021).
[14] Y. Qi and A. M. Rappe, Phys. Rev. Lett. **126**, 217601 (2021).
[15] L. You, Y. Zhang, S. Zhou, A. Chaturvedi, S. A. Morris, F. Liu, L. Chang, D. Ichinose, H. Funakubo, and W. Hu, Sci. Adv. **5**, eaav3780 (2019).
[16] M. Si, A. K. Saha, P.-Y. Liao, S. Gao, S. M. Neumayer, J. Jian, J. Qin, N. Balke Wisinger, H. Wang, and P. Maksymovych, ACS Nano **13**, 8760 (2019).
[17] V. Maisonneuve, V. B. Cajole, A. Simon, R. Von Der Mull, and J. Raves, Phys. Rev. B **56**, 10860 (1997).
[18] See Supplemental Material at http://link.aps.org/supplemental/10.1103/PhysRevB.107.045406 for additional data and details on the experiments.
[19] K. Takenaka and H. Takagi, Appl. Phys. Lett. **87**, 261902 (2005).
[20] V. Nicolosi, M. Chowilla, M. G. Anatids, M. S. Strand, and J. N. Coleman, Science **340**, 1226419 (2013).
[21] L. Neu, F. Liu, Q. Zeng, X. Zhu, Y. Wang, P. Yu, J. Shi, J. Lin, J. Zhou, and Q. Fu, Nano Energy **58**, 596 (2019).
[22] D.-D. Xu, R.-R. Ma, A.-P. Fu, Z. Guan, N. Zhong, H. Peng, P.-H. Xiang, and C.-G. Duan, Nat. Commun. **12**, 655 (2021).
[23] D.-D. Xu, R.-R. Ma, Y.-F. Zhao, Z. Guan, Q.-L. Zhong, R. Huang, P.-H. Xiang, N. Zhong, and C.-G. Duan, J. Mater. Chem. C **8**, 6966 (2020).
[24] Y. M. Vysotskaya, V. A. Stipanovich, A. A. Molnar, V. B. Cajole, and X. Bourdon, Phys. Rev. B **58**, 9119 (1998).
[25] A. Daegu's, J. Bans, J. Masseteric, R. Sebastiana's, and Y. Vysochanskii, Phys. Status Solid A **207**, 1960 (2010).
[26] S. Zhou, L. You, A. Chaturvedi, S. A. Morris, J. S. Herrin, N. Zhang, A. Abdelsamie, Y. Hu, J. Chen, Y. Zhou, S. Dong, and J. Wang, Mater. Horiz. **7**, 263 (2020).